Journal of Manufacturing Innovations
2024, VOL. 1, NO. 2, 17-27
DOI: 10.22055/jomi.2024.46908.1015

Modeling metal forming processes using an Updated Lagrangian smoothed particle hydrodynamics method

Hojjat Badnava*

Department of Mechanical Engineering, Behbahan Khatam Alanbia University of Technology, Behbahan, Iran

ABSTRACT

In this research, the Smoothed Particle Hydrodynamics (SPH) method has been used to model the dynamic behavior of solids under large deformation. In this regard, a set of combined equations for linear momentum, deformation gradient tensor, volume mapping, and area mapping (the co-factor of the deformation gradient tensor) is derived in form of first-order conservation laws. Subsequently, the corrected SPH method has been employed for spatial discretization within the solution domain. To reduce computational costs, explicit temporal discretization is considered using the third-order Runge-Kutta method. In the SPH meshless method, neighboring point information is utilized for computations. The primary objective of employing these equations in Updated Lagrangian description, where neighboring points may change at each time step, is enabling the simulation of severe deformation, which poses challenges for mesh-based approaches. Hence, the modeling capability of the proposed numerical method is examined by simulating the behavior of materials undergoing severe plastic deformation in the forging process. The simulation of the necking example demonstrates the model's capability to predict plastic behavior accompanied by large deformations. Additionally, simulation in the forging process accompanied by very large and complex deformations showed that the proposed meshless model can simulate such deformations without the need for ALE formulation or remeshing.

ARTICLE HISTORY
Received 14 May 2024
Revised 1 June 2024
Accepted 17 June 2024

KEYWORDS
Smoothed particle hydrodynamics
Meshless method
Forging
Large deformation

1. Introduction

Forming processes are always accompanied by large deformations and consequently large strains. Simulating forming processes based on mesh-based methods, including finite element method, requires mesh updating or adaptive meshing based on Arbitrary Lagrangian-Eulerian (ALE) formulations. Both of these approaches are computationally complex and have high computational costs. In meshless methods, computations are based on points values, which is a significant advantage, especially in simulating processes with severe deformations. Particle-based methods can perform particle corrections in a more efficient manner, as the interpolation of the response to connect elements is not dependent on the existence of elements. However, the complexity of particle corrections remains a challenging aspect of this method. Additionally, meshless methods provide easier numerical implementation in three-dimensional cases compared to mesh-based methods.

In most meshless methods, the approximation of variables and their derivatives is performed based on the values available at neighboring points and using a weighting function. The first meshless method is SPH, initially proposed by Gingold and Monaghan [1,2] for solving problems in computational physics. Monaghan and his colleagues have extended this method to computational mechanics problems [3–5]. Another meshless computational method is the Reproducing Kernel Particle Method (RKPM), which utilizes a weighting function, and its applications in computational mechanics can be found in references [6,7]. The use of the least squares minimization method is another approach to construct shape function, which first introduced in meshless methods by Nayroles [8], and later expanded by Belytschko and his colleagues under the name of Element-Free Galerkin (EFG) method [9–12]. The traditional SPH method is always

* Corresponding author.
E-mail address: Badnava@bkatu.ac.ir (H.Badnava)

prone to instability. To address this issue, Bonet and Kulasegaram [13] modified the shape function to enforce stability conditions and improve accuracy. The modified SPH method with shape functions has been used to simplify the process. It has also been noted that integration at points in the modified SPH method still suffers from instabilities. These spatial instabilities resulting from the integration of the weakened form of the shape function are mitigated using the least squares stabilizing method. Belytschko and his colleagues [14], after stability analysis of particle-based methods, stated that using a Lagrangian kernels and the stress points methods are the best approaches for discretizing particle-based algorithms. In fact, using Lagrangian-based kernels can eliminate tensile instability while having energy-free modes.

Based on the capabilities of meshless methods, they can be used in simulating and analyzing metal forming and manufacturing processes. Alfano and colleagues [15] have studied the applications of meshless methods in metal forming. They investigated the natural element method in simulating forming processes involving large deformations. Their aim was to address the issue arising from boundary condition enforcement due to the failure of satisfying the Kronecker delta condition in most meshless methods. Xiong and co-workers [16] utilized the reproducing kernel particle method for analyzing bulk metal forming processes. They examined the capability of this method in simulating processes such as flat rolling, heading of cylindrical billets, and rod compression, comparing results with analytical, finite element analysis, and experimental results to assess the effectiveness of meshless methods, demonstrating that meshless methods can simulate severe plastic deformation without the need for remeshing. In another study, Xiong and colleagues [17] investigated the use of background cells in the reproducing kernel particle method for bulk metal forming applications. Chinesta and Cueto [18] reviewed the characteristics and capabilities of meshless methods, studying their usability in material forming simulation by examining their advantages and limitations. Costa and colleagues [19] simulated and optimized the extrusion process using the point interpolation meshless method, focusing on its accuracy and stability and providing guidelines for extrusion simulation with this method.

Lee and co-workers [20] studied the application of meshless methods in simulating the additive manufacturing process for samples with complex and unusual geometries. They used meshless methods to create layers in additive manufacturing and compared simulation results with incrementally manufactured samples. Zhang and colleagues [21] utilized the smoothed particle hydrodynamics (SPH) method for simulating the cold spray additive manufacturing process. Chhillar and colleagues [22] used meshless methods to analyze the elastic-plastic behavior of metal parts during forming processes, investigating the effect of different weight functions on result accuracy. Another similar study is by Redrigues and colleagues [23], who employed the radial point interpolation meshless method to analyze the bending of laminates using high-order shear deformation theory.

In numerical simulations of elastoplastic behavior in the presence of large deformations or hyperelastic materials, incompressibility conditions lead to volumetric locking and non-physical pressure distributions. Various methods have been proposed to overcome this issue. One of these methods is the mixed-based formulation methodology, which has been implemented in recent years using different numerical method including finite element, finite volume Element free Galerkin, and SPH methods [24,25,34,26–33]. In metal forming processes, such as forging, large deformations in the material lead to challenging issues in numerical simulations using mesh-based methods. Numerical simulation of such a problems encounter difficulty once a certain level of distortion in the elements is reached unless an appropriate mesh refinement is applied to deal with the distortions resulting from sever deformation. The problem of element distortion and consequently, remeshing, is the subject of many research in the field of mesh-based methods. By utilizing meshless numerical frameworks, these challenges can be overcome.

In this study, a set of first-order conservation laws for linear momentum, the deformation gradient tensor, the area mapping tensor, and the volume mapping (determinant of the deformation gradient tensor) are derived in form of Updated Lagrangian description. The updated description means that neighboring particles of each target particle are recalculated at each solution step based on their new positions. After the change in the positions of

neighboring particles, it is necessary to update the shape functions and the gradient operator in the proposed meshless method. Therefore, the capability of modeling severe deformations using the proposed meshless method without encountering the issues arising from limited mesh adaptation has been developed. In addition, the modified SPH method is utilized for discretizing the mentioned conservation laws. Finally, the set of equations is explicitly solved using a third-order Runge-Kutta time integration approach. The modeling capability of the proposed method in the presence of large deformations and incompressible conditions is investigated through simulating the forging process.

2. Materials and Methods

2-1- Updated Lagrangian conservation laws

The motion of a three-dimensional body, assuming constant temperature, from initial configuration with density ρ_0, volume Ω_R, with boundary $\partial\Omega_R$ to current deformed configuration with volume Ω and boundary $\partial\Omega$ over a period of time t is considered according to Figure (1). The deformation of the body occurs through a one-to-one mapping $\boldsymbol{x} = \boldsymbol{\phi}(\boldsymbol{X}, t)$ from initial coordinates $\boldsymbol{X}$ to current coordinates $\boldsymbol{x}$. For the body in question, the deformation gradient tensor, $\boldsymbol{F}$, is defined as follows:

$$\boldsymbol{F} = \boldsymbol{\nabla}_0 \boldsymbol{\phi}(\boldsymbol{X}, t) = \frac{\partial \boldsymbol{\phi}(\boldsymbol{X},t)}{\partial \boldsymbol{X}} \quad (1)$$

where the operator $\boldsymbol{\nabla}_0$ represents the material gradient. Additionally, the velocity $\boldsymbol{v}(\boldsymbol{X}, t)$, linear momentum $\boldsymbol{p}(\boldsymbol{X}, t)$, area mapping $\boldsymbol{H}$, and volume mapping J are expressed as follows:

$$J = det(\boldsymbol{F}) = \frac{dv}{dV} \quad (2)$$

$$\boldsymbol{H} = \frac{1}{2}\, \boldsymbol{F} \times \boldsymbol{F} \quad (3)$$

$$\boldsymbol{v}(\boldsymbol{X}, t) = \frac{\partial \boldsymbol{\phi}(\boldsymbol{X},t)}{\partial t} \quad (4)$$

$$\boldsymbol{p}(\boldsymbol{X}, t) = \rho_0 \boldsymbol{v}(\boldsymbol{X}, t) \quad (5)$$

where the symbol × denotes tensor multiplication. In this case, the conservation laws are expressed locally and in the Updated Lagrangian description as [25,34–37],

$$\frac{\partial \boldsymbol{p}}{\partial t} - div_{\boldsymbol{x}} \boldsymbol{\sigma} = \boldsymbol{b} \quad (6)$$

$$\frac{\partial \boldsymbol{f}}{\partial \mathrm{t}} - \mathrm{div}_{\mathbf{x}}(\boldsymbol{v} \otimes \boldsymbol{i}) = \boldsymbol{0} \quad (7)$$

$$\frac{\partial \boldsymbol{h}}{\partial \mathrm{t}} - curl_{\mathbf{x}}(\boldsymbol{v} \times \boldsymbol{f}) = \boldsymbol{0} \quad (8)$$

$$\frac{\partial j}{\partial \mathrm{t}} - \mathrm{div}_{\mathbf{x}}(\boldsymbol{h}^T \boldsymbol{v}) = 0 \quad (9)$$

In these equations, $\boldsymbol{b}$ represents the volumetric force, $\boldsymbol{\sigma}$ denotes the Cauchy stress tensor, $curl_{\mathbf{x}}$ and $\mathrm{div}_{\mathbf{x}}$ refer to the spatial curl and divergence, respectively. $\boldsymbol{f}$, $\boldsymbol{h}$, and J represent the nodal values of the gradient of deformation, area mapping, and volume mapping, respectively, defined between two solution steps from n to $n+1$ as follows:

$$\boldsymbol{F}_{n+1} = \boldsymbol{f}\boldsymbol{F}_n; \quad \boldsymbol{H}_{n+1} = \boldsymbol{h}\boldsymbol{H}_n; \quad J_{n+1} = jJ_n \quad (10)$$

The above equations are expressed as first-order conservation laws, which, by considering the general conservation variable $\boldsymbol{\mathcal{U}}$, flux $\boldsymbol{\mathcal{F}}_I$, and source term $\boldsymbol{\mathcal{S}}$, can be rewritten as a set of equations in a compact form as follows:

$$\boldsymbol{\mathcal{U}} = \begin{bmatrix} \boldsymbol{p} \\ \boldsymbol{f} \\ \boldsymbol{h} \\ j \end{bmatrix}; \quad \boldsymbol{\mathcal{F}}_I = -\begin{bmatrix} \boldsymbol{\sigma e}_I \\ \boldsymbol{v} \otimes \boldsymbol{e}_I \\ \boldsymbol{f} \times (\boldsymbol{v} \otimes \boldsymbol{e}_I) \\ \boldsymbol{h} : (\boldsymbol{v} \otimes \boldsymbol{e}_I) \end{bmatrix}; \quad \boldsymbol{\mathcal{S}} = \begin{bmatrix} \boldsymbol{b} \\ \boldsymbol{0} \\ \boldsymbol{0} \\ 0 \end{bmatrix} \quad (11)$$

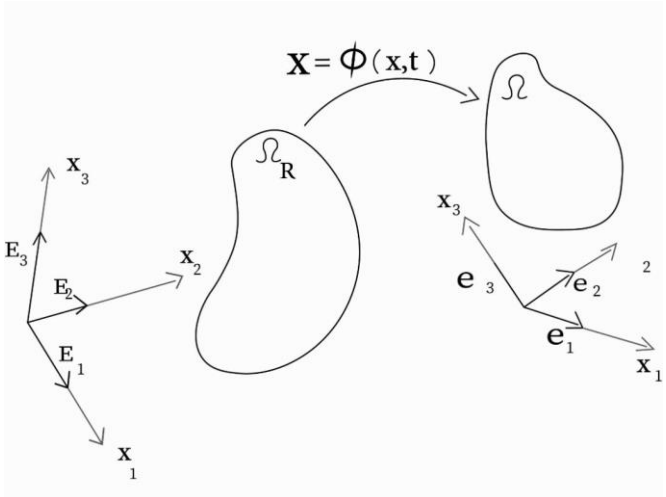

Figure 1. Motion of a deformable three-dimensional body.

With the standard approach, the weak form of the above equations can be obtained as follows [29],

$$\int_\Omega \delta \boldsymbol{v} \cdot \frac{\partial \boldsymbol{p}}{\partial t} dV = -\int_\Omega \boldsymbol{\sigma} : \boldsymbol{\nabla}_x \delta \boldsymbol{v} dV + \int_\Omega \delta \boldsymbol{v} \cdot \boldsymbol{b}\, dV + \int_{\partial\Omega} \delta \boldsymbol{v} \cdot \boldsymbol{t} da \quad (12)$$

$$\int_\Omega \delta \boldsymbol{\Sigma}_{\boldsymbol{f}} : \frac{\partial \boldsymbol{f}}{\partial t} dV = \int_\Omega \delta \boldsymbol{\Sigma}_{\boldsymbol{f}} : \boldsymbol{\nabla}_x \boldsymbol{v} dV \quad (13)$$

$$\int_\Omega \delta \boldsymbol{\Sigma}_{\boldsymbol{h}} : \frac{\partial \boldsymbol{h}}{\partial t} dV = \int_\Omega \delta \boldsymbol{\Sigma}_{\boldsymbol{h}} : (\boldsymbol{f} \times \boldsymbol{\nabla}_x \boldsymbol{v}) dV \quad (14)$$

$$\int_\Omega \delta \Sigma_j : \frac{\partial j}{\partial t} dV = \int_\Omega \delta \Sigma_j\, \boldsymbol{h} : \boldsymbol{\nabla}_x \boldsymbol{v}\, dV \quad (15)$$

where $\boldsymbol{t}$ is the surface traction vector, and $\delta \boldsymbol{\Sigma}_{\boldsymbol{f}}$, $\delta \boldsymbol{\Sigma}_{\boldsymbol{h}}$, and $\delta \Sigma_j$ are the virtual work conjugates of the stresses $\boldsymbol{\Sigma}_{\boldsymbol{f}}$, $\boldsymbol{\Sigma}_{\boldsymbol{h}}$, and Σ_j respectively.

2.2. Spatial discretization using the SPH method

To compute the value or gradient of any desired vector function $\boldsymbol{T}$, the gradient approximation of this function at a target particle at position $\boldsymbol{x}_a$ is considered. Particles within a specific range around the selected particle, denoted as Λ_a^b are taken into account. The value of the function is considered at points surrounding the target particle, and the value and gradient are calculated at the selected target point.

$$\boldsymbol{T}(\boldsymbol{x}_a) = \sum_{b\epsilon\Lambda_a^b} V_b \boldsymbol{T}_b w_b(\boldsymbol{x}_a) \quad (16)$$

$$\boldsymbol{\nabla}_{\boldsymbol{x}}\boldsymbol{T}(\boldsymbol{x}_a) = \sum_{b\epsilon\Lambda_a^b} V_b(\boldsymbol{T}_b - \boldsymbol{T}_a)\otimes\tilde{\boldsymbol{\nabla}} w_b(\boldsymbol{x}_a) \quad (17)$$

In the above equations, w represents the weight function, V_b denotes the weight of point b, and $\tilde{\boldsymbol{\nabla}}$ represents the corrected gradient [28]. Using the above definitions, the discrete form of the weak statement can be derived as,

$$V_a\frac{d\boldsymbol{p}_a}{dt} = \sum_{b\epsilon\Lambda_a^b}\frac{1}{2}(\boldsymbol{\sigma}_a\boldsymbol{g}_{ab} - \boldsymbol{\sigma}_b\boldsymbol{g}_{ba}) + \sum_{b\epsilon\Lambda_a^b}\boldsymbol{D}_{ab}^p + V_a\boldsymbol{b}_a + A_a\boldsymbol{t}_a \quad (18)$$

$$V_a\frac{df_a}{dt} = \sum_{b\epsilon\Lambda_a^b}\frac{1}{2}(\boldsymbol{v}_b - \boldsymbol{v}_a)\otimes\boldsymbol{g}_{ab} \quad (19)$$

$$V_a\frac{d\boldsymbol{h}_a}{dt} = \boldsymbol{f}_a \times \left(\sum_{b\epsilon\Lambda_a^b}\frac{1}{2}(\boldsymbol{v}_b - \boldsymbol{v}_a)\otimes\boldsymbol{g}_{ab}\right) \quad (20)$$

$$V_a\frac{dj_a}{dt} = \boldsymbol{h}_a : \left(\sum_{b\epsilon\Lambda_a^b}\frac{1}{2}(\boldsymbol{v}_b - \boldsymbol{v}_a)\otimes\boldsymbol{g}_{ab}\right) + \sum_{b\epsilon\Lambda_a^b} D_{ab}^j \quad (21)$$

where,

$$\boldsymbol{g}_{ab} = 2V_aV_b\tilde{\boldsymbol{\nabla}}w_b(\boldsymbol{x}_a);\ \boldsymbol{g}_{ba} = 2V_aV_b\tilde{\boldsymbol{\nabla}}w_a(\boldsymbol{x}_b) \quad (22)$$

$$\boldsymbol{D}_{ab}^p = \boldsymbol{S}_{ab}^p(\boldsymbol{v}_{ab}^R - \boldsymbol{v}_{ab}^L);\quad D_{ab}^j = S_{ab}^j(\Sigma_{j,ab}^R - \Sigma_{j,ab}^L) \quad (23)$$

$$\boldsymbol{S}_{ab}^p = \frac{\rho_{ab}^{ave}\left\|\boldsymbol{g}_{ab}^{skew}\right\|}{2}\left[c_p^{ave}\boldsymbol{n}_{ab}\otimes\boldsymbol{n}_{ab} + c_s^{ave}(\boldsymbol{I} - \boldsymbol{n}_{ab}\otimes\boldsymbol{n}_{ab})\right] \quad (24)$$

$$S_{ab}^j = \frac{\boldsymbol{g}_{ab}^{ave}\cdot\boldsymbol{g}_{ab}^{skew}}{2\rho_{ab}^{ave}c_{p.ab}^{ave}\left\|\boldsymbol{g}_{ab}^{skew}\right\|} \quad (25)$$

$$\boldsymbol{n}_{ab} = \frac{\boldsymbol{x}_b - \boldsymbol{x}_a}{\|\boldsymbol{x}_b - \boldsymbol{x}_a\|} \quad (26)$$

In these equations, c_p and c_s represent the speeds of pressure and shear waves within the material, respectively, and the superscripts L and R denote the left and right values along the line between two neighboring particles in the linear reconstruction process [25]. Linear reconstruction leads to energy dissipation reduction in stabilizing the dynamic response with the proposed method. It should be noted that D^j and $\boldsymbol{D}^p$ are stabilized terms for the volume mapping and linear momentum conservation laws, respectively, which are generated using a Riemann solver [30].

2.3. Explicit time integration

The set of combined equations presented is solved explicitly using the three-stage Runge-Kutta integration method. In this method, the variable $\boldsymbol{U}$ is updated in the time step $\Delta t = t_{n+1} - t_n$ as follows [29,33],

$$\boldsymbol{U}_a^* = \boldsymbol{U}_a^n + \Delta t\dot{\boldsymbol{U}}_a^n(\boldsymbol{U}_a^n) \quad (27)$$

$$\boldsymbol{U}_a^{**} = \frac{3}{4}\boldsymbol{U}_a^n + \frac{1}{4}\left(\boldsymbol{U}_a^* + \Delta t\dot{\boldsymbol{U}}_a^*(\boldsymbol{U}_a^*)\right) \quad (28)$$

$$\boldsymbol{U}_a^{n+1} = \frac{1}{3}\boldsymbol{U}_a^n + \frac{2}{3}\left(\boldsymbol{U}_a^{**} + \Delta t\dot{\boldsymbol{U}}_a^{**}(\boldsymbol{U}_a^{**})\right) \quad (29)$$

Explicit solution, unlike implicit solution, is not stable, and the time step must be chosen in a way that ensures the stability of the problem. This is governed by the speed of the pressure wave inside the body, for which the Courant-Friedrichs-Lewy (CFL) condition is used in the following form [38],

$$\Delta t = \alpha_{CFL}\min\left(\frac{\|\boldsymbol{x}_a - \boldsymbol{x}_b\|}{c_p^{ave}}\right) \quad (30)$$

where α_{CFL} is the Courant-Friedrichs-Lewy stability coefficient. In this study, a value of $\alpha_{CFL} = 0.3$ has been used.

2.4. Elastic-plastic constitutive model

The elastic-plastic behavior considered in this study assumes multiplication decomposition of the deformation gradient tensor, $\boldsymbol{F}$, based on the intermediate configuration concept [39],

$$\boldsymbol{F}(\boldsymbol{X},t) = \boldsymbol{F}^e(\boldsymbol{X},t)\,\boldsymbol{F}^p(\boldsymbol{X},t) \quad (31)$$

in which $\boldsymbol{F}^e$ and $\boldsymbol{F}^p$ are elastic and plastic parts of the deformation gradient tensor, respectively. The left and right Cauchy-Green strain tensors can be defined as,

$$\boldsymbol{C}^p = \boldsymbol{F}^{p^T}\boldsymbol{F}^p,\ \boldsymbol{B}^e = \boldsymbol{F}^e\boldsymbol{F}^{e^T} \quad (32)$$

Based on equations (31) and (32), the following relation can be derived,

$$\boldsymbol{B}^e = \boldsymbol{F}\boldsymbol{F}^{p^{-1}}\boldsymbol{F}^{p^{-T}}\boldsymbol{F}^T = \boldsymbol{F}\left[\boldsymbol{F}^{p^T}\boldsymbol{F}^p\right]^{-1}\boldsymbol{F}^T = \boldsymbol{F}\boldsymbol{C}^{p^{-1}}\boldsymbol{F}^T \quad (33)$$

Assuming isotropic material behavior and based on the idea of multiplication decomposition and the absence of stress in the intermediate configuration, the stress-strain response can be extracted from the following energy equation,

$$W = \frac{1}{2}G(tr[\bar{\boldsymbol{B}}^e] - 3) + \frac{1}{2}K\left[\frac{1}{2}\left(J^{e^2} - 1\right) - lnJ^e\right] \quad (34)$$

$$\bar{\boldsymbol{B}}^e = J^{e^{-2/3}}\boldsymbol{F}^{-e}\boldsymbol{F}^{e^T} = J^{e^{-2/3}}\boldsymbol{B}^e \quad (35)$$

According to the above equation, the stress is calculated as follows,

$$\boldsymbol{\tau} = 2\boldsymbol{F}^e \frac{\partial W}{\partial \boldsymbol{C}^e} \boldsymbol{F}^{e^T} = J^e p \boldsymbol{I} + \boldsymbol{S} \quad (36)$$

$$p = \frac{K}{2}\frac{(J^{e^2}-1)}{J^e} \quad (37)$$

$$\boldsymbol{S} = dev[\boldsymbol{\tau}] = G\ dev\ [\bar{\boldsymbol{B}}^e] \quad (38)$$

Where $\boldsymbol{\tau}$, p and $\boldsymbol{S}$ are the Kirchhoff stress tensor, pressure, and deviatoric part of the Kirchhoff stress tensor, respectively. It should be noted that, according to the yield stress criterion, the yield limit can be estimated using the Mises equation for the yield surface,

$$f(\boldsymbol{\tau}, \bar{\varepsilon}^p) = \|\boldsymbol{S}\| - \sqrt{\frac{2}{3}}\,[\tau_y^0 + H\,\bar{\varepsilon}^p] \quad (39)$$

Where τ_y^0 is the initial yield stress and H is the hardening/softening slope where can be a function of the equivalent plastic strain. The integration algorithm for the above constitutive model is described in appendix A.

3. Results and Discussion

In this section, the results of the analysis of two different models of forging using the proposed solution framework are presented. In both examples, the material behavior is assumed to be elastoplastic with linear hardening. In addition, a benchmark example. Necking of a circular bar, is investigated to demonstrate the ability of the proposed algorithm in modelling sever localized plastic deformation.

3.1. Necking benchmark test

In this section, a benchmark example extensively used for validating and assessing the accuracy of numerical solutions in simulating plastic deformation within the range of finite strain is considered [40,41].

Table 1. Material parameters for necking of a circular bar [40,41].

Material density	ρ_R	$7850\ kg/m^3$
Young modulus	E	$117\ GPa$
Poisson ratio	ϑ	0.35
Initial yield stress	τ_y^0	$450\ MPa$
Saturation yield stress	τ_y^∞	$715\ MPa$
Hardening exponent	δ	16.93
Linear hardening modulus	H	$129.24\ MPa$

This example simulates the necking process of a cylindrical rod. The geometry consists of a rod with a circular cross-section with a radius of 6.413 mm and a length of 53.34 mm. The geometry of the specimen is shown in Figure (2). To induce localized deformation in the specimen, a small change in diameter in the middle section is considered, continuing linearly up to half of the specimen. Due to symmetry, only a quarter of the specimen is considered in the simulation to reduce computational costs. In all reference articles, nonlinear hardening behavior is considered for this simulation, where the yield stress changes according to the equation,

$$\tau_y(\bar{\varepsilon}_p) = \tau_y^0 + H\bar{\varepsilon}_p + (\tau_y^\infty - \tau_y^0)[1 - e^{-\delta\bar{\varepsilon}_p}] \quad (40)$$

Here, H is the hardening modulus, τ_y^∞ is the saturated yield stress, and δ is the hardening exponent. The coefficients used in this simulation are presented in Table (1). The main objective of this example is to induce severe localized deformation within the body.

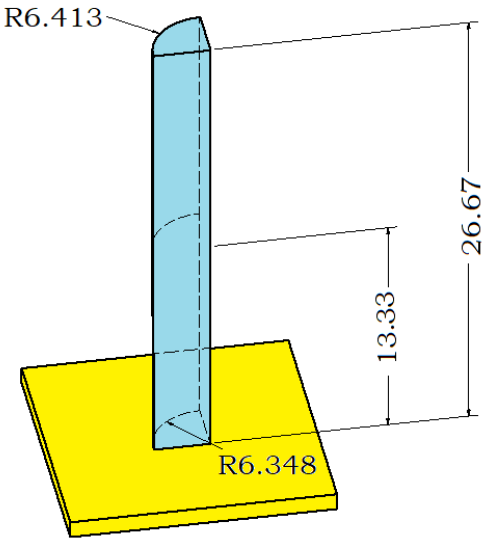

Figure 2. Geometry for the quarter of the necking bar sample.

Evolution of the diameter of the specimen during the necking process are considered as a criterion for the accuracy of numerical solutions in this example. In Figure (3), the final deformation of the specimen along with the equivalent plastic strain distribution and the distribution of von Mises stress are shown. To quantitatively assess the accuracy of the solution, changes in the diameter of the specimen in the necking zone as a function of its length are shown in Figure (4). The obtained results are compared with experimental and numerical results from various references in Figure (4), indicating a good agreement, demonstrating the accuracy of the equations and implementation in the proposed numerical method.

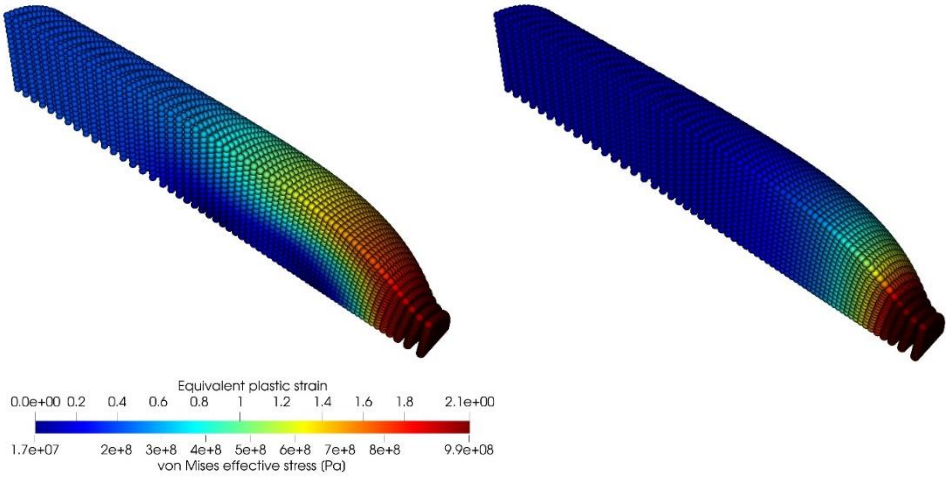

Figure 3. Three-dimensional demonstration of the deformed sample with von Mises effective stress contour (left) and effective plastic strain distribution (right).

3.2. Forging a circular plate

This example is taken from reference [35]. In the mentioned reference, this sample has been simulated using the finite element numerical solution method. In this study, the sample is modeled using the proposed meshless method.

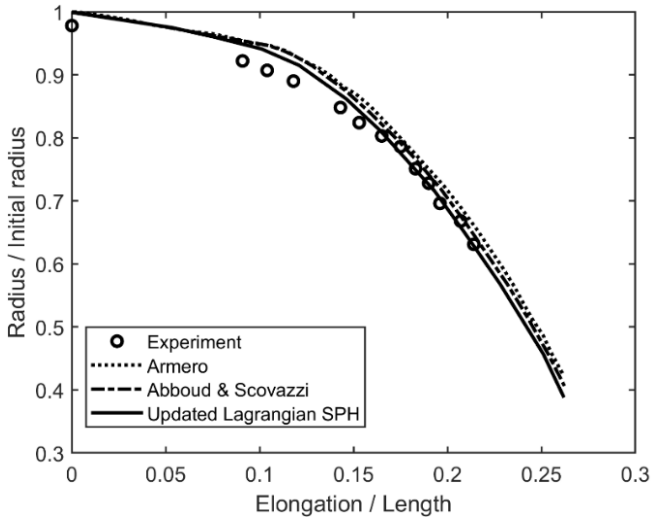

Figure 4. Normalized bar radius at the necking area versus normalized elongation [40,41].

The simulation involves analyzing the deformation of a circular sheet with a radius of 80 millimeters and a height of 32 millimeters, as shown in Figure (5), subjected to compression. The material coefficients that used in the forging examples are provided in Table (2). The upward velocity of the mold is $v = 100\ mm/s$, and the simulation is conducted over a period of 0.2 s, resulting in a displacement of the die of 20 mm. In Figure (6), the stages of deformation of the sample during loading along with the distribution of equivalent plastic strain and pressure are illustrated. In the simulation, plastic behavior with large deformations leads to incorrect and oscillatory distribution of pressure based on traditional displacement-based equations. In the equations presented in this study, the stabilizing component included in the equation governing the rate of change of the volume mapping has a key effect on solving this problem. As shown in Figure (6), the pressure distribution is smooth and free from oscillations and checkerboard patterns.

Table 2. Material behavior coefficients [35].

Density	ρ_R	$8930\ kg/m^3$
Young's modulus	E	$117\ GPa$
Poisson's ratio	ϑ	0.35
Initial yield stress	τ_y^0	$400\ MPa$
Hardening modulus	H	$100\ MPa$

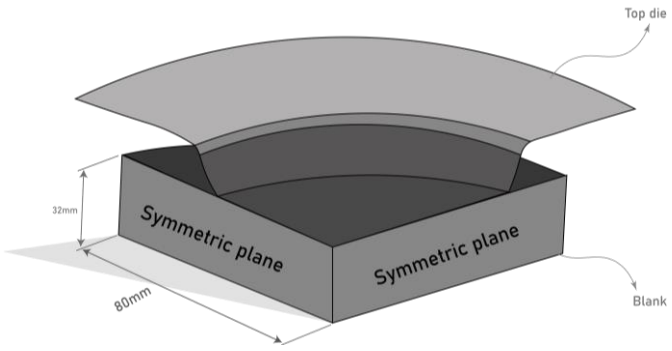

Figure 5. Dies views and sample dimension in circular disk forging.

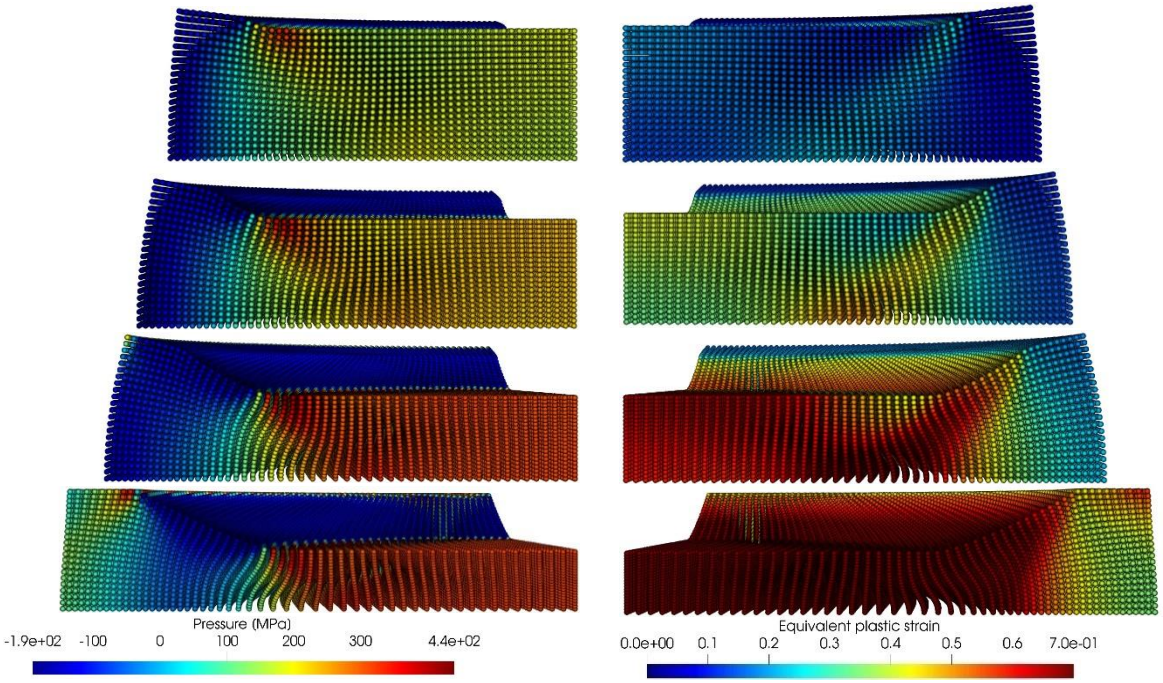

Figure 6. Various stages of plate deformation in the forming process at times {0.05, 0.1, 0.15, 0.2} seconds along with pressure distribution (left column) and equivalent plastic strain (right column).

3.3. Forging with complex dies

This section presents the analysis of the forming process of a component using the forging method and two dies with complex geometry. The analysis is adapted from reference [36], which aims to apply finite element methods in the field of forging industries. In this study, the desired with a complex mold at times {0.025, 0.05, 0.075, 0.1} seconds are illustrated. Additionally, in Figure (8), the distribution of displacement and equivalent plastic strain at different stages of deformation is presented. The results demonstrate that the proposed model effectively simulates complex processes with large deformations without any additional efforts to eliminate mesh distortion induced by sever deformation.

Finally, in order to validate the results obtained using the proposed method, a comparison is made between the obtained results and the one is simulated by finite element solution using the ALE formulation with the commercial software Abaqus using the reduced integration hexahedral elements. Figure (9) depicts the contour plot for

model, illustrated in Figure (7), is simulated using the meshless method based on the provided equations. The simulation of the forging process involves the movement of the top die at a constant speed of 166.65 mm/s, and the simulation is conducted over a period of 0.1 s.

In Figure (5), various stages of deformation in the forging process

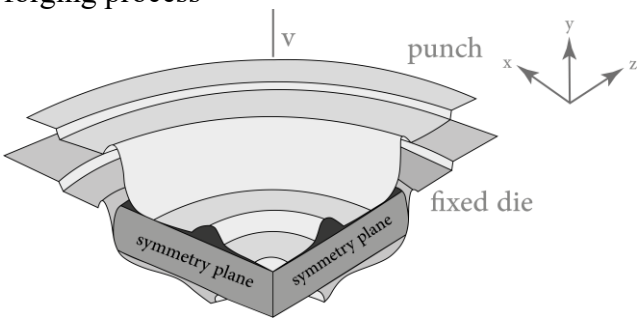

Figure 7. Views of the dies and sample in forming with complex dies.

displacement and the equivalent plastic strain at simulation time 0.97 s. As shown, the SPH results agree extremely well with those obtained using the FEM method.

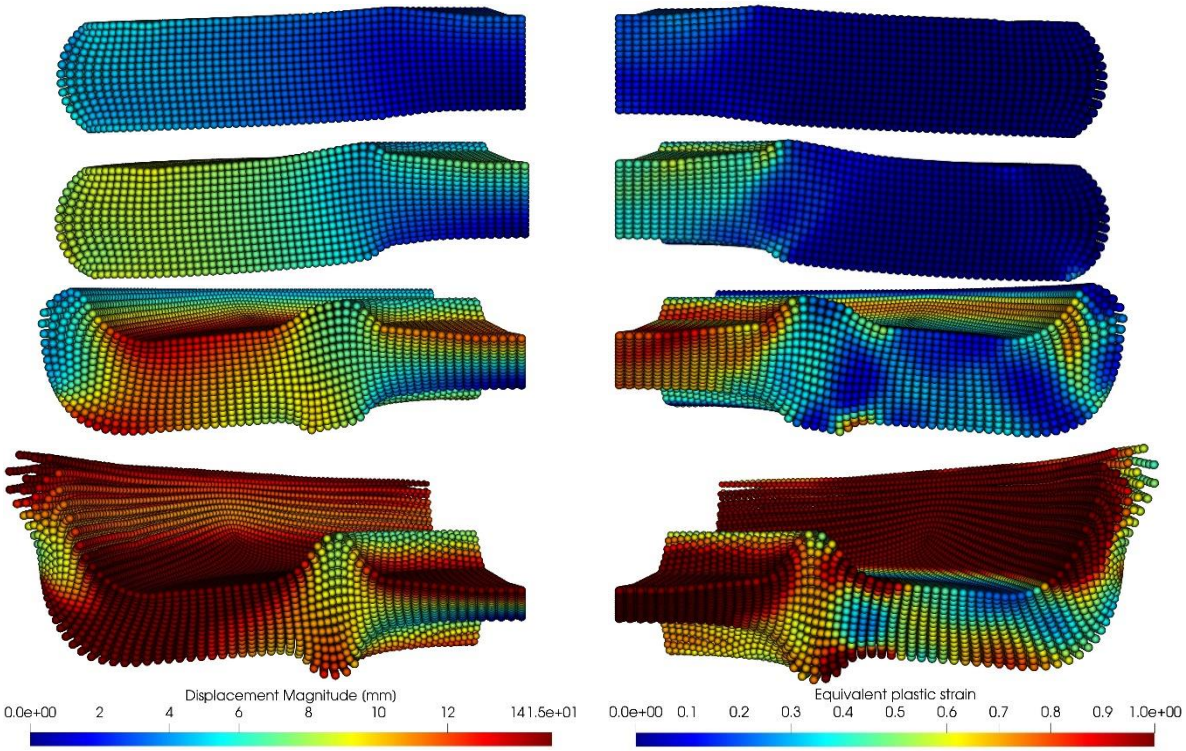

Figure 8. Different stages of deformation in the forming process with complex dies at times {0.025, 0.05, 0.075, 0.1} seconds along with displacement distribution (left column) and equivalent plastic strain (right column)

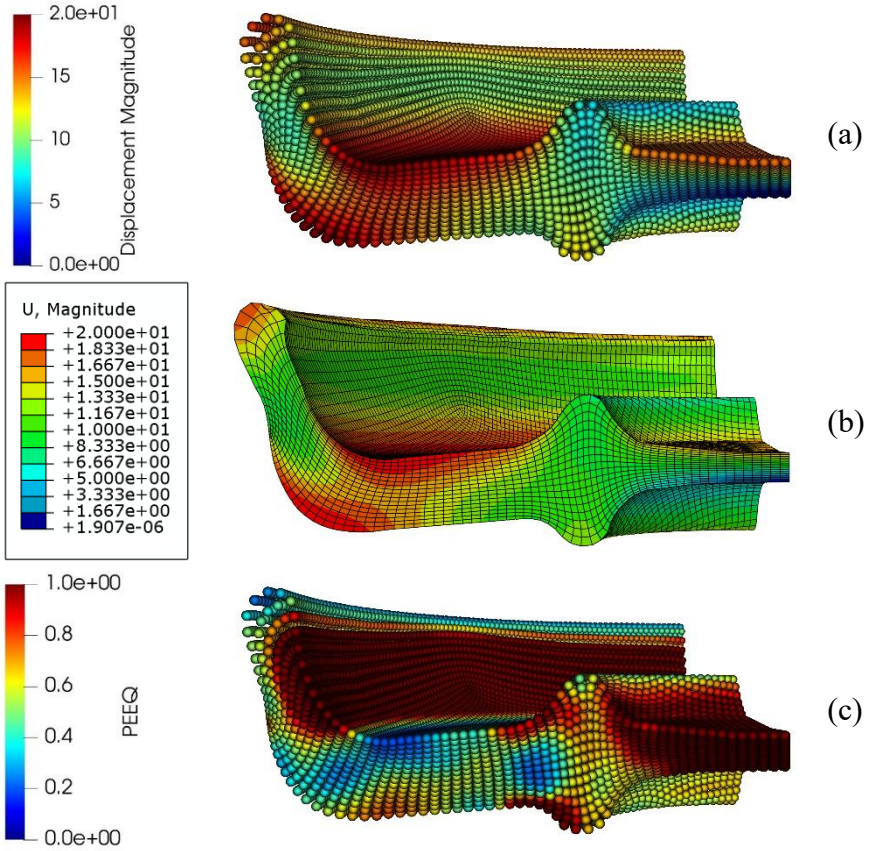

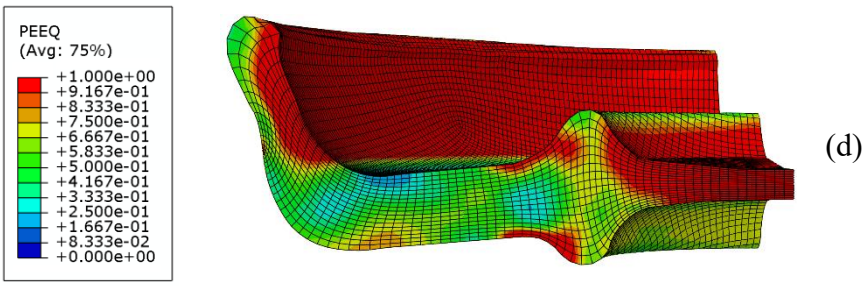

Figure 9. Comparison between SPH results and finite element simulation obtained by Abaqus software. displacement contour plot by (a) SPH and (b) FEM, equivalent plastic strain (PEEQ) obtained by (c) SPH and (d) FEM.

4. Conclusions

In this study, the implementation of combined relations in the form of first-order conservation laws for linear momentum, strain gradient, surface mapping, and volume mapping using Smoothed Particle Hydrodynamics (SPH) method was described. The updated Lagrangian-based equations were presented, where neighboring particles change with deformation, enabling the modeling of very large deformations without the need for mesh regeneration or adaptive mesh refinement (ALE). The capability of the proposed approach was examined through simulating the forging process. The results demonstrated that the proposed model can effectively simulate smooth pressure distributions and overcome the pressure checkerboard artifact commonly observed in displacement-based solutions.

Appendix

A. Integration algorithm for the von Mises J2 plasticity model

The standard return mapping algorithm to integrate the Kirchhoff stress tensor based on the a von Mises type plasticity model is described here for completeness in Algorithm 1 [39].

Algorithm 1. Return mapping algorithm for the standard J2 plasticity

1. Obtain the input $\{\boldsymbol{F}_{n+1}, J_{n+1}, \boldsymbol{C}_n^{P^{-1}}, \bar{\varepsilon}_n^P\}$

2. Compute elastic trial values

$$\boldsymbol{B}_{n+1}^{e\,trial} = \boldsymbol{F}_{n+1}\boldsymbol{C}_n^{P^{-1}}\boldsymbol{F}_{n+1}^T$$

$$\boldsymbol{S}_{n+1}^{trial} = G\,dev\left[\bar{\boldsymbol{B}}_{n+1}^{e\,trial}\right]$$

$$p_{n+1}^{trial} = p_{n+1} = \frac{K}{2}\frac{(J_{n+1}^{e^2}-1)}{J_{n+1}^e}$$

3. Check yield condition using the trial stress

$$f_{n+1}^{trial} = \left\|\boldsymbol{S}_{n+1}^{trial}\right\| - \sqrt{\frac{2}{3}}\,[\tau_y^0 + H\,\bar{\varepsilon}_n^P]$$

IF $f_{n+1}^{trial} \le 0$

Elastic step, set $(\cdot)_{n+1} = (\cdot)_{n+1}^{trial}$

ELSE

Go to the next step for return mapping.

4. The return mapping step

Compute $\Delta\gamma$ using an iterative method

$$\boldsymbol{S}_{n+1} = \boldsymbol{S}_{n+1}^{trial} - 2\bar{G}\Delta\gamma\boldsymbol{n}$$

$$\boldsymbol{n} = \frac{\boldsymbol{S}_{n+1}^{trial}}{\left\|\boldsymbol{S}_{n+1}^{trial}\right\|},\ \bar{G} = \frac{1}{3}tr\left(\bar{\boldsymbol{B}}_{n+1}^{e\,trial}\right)G$$

5. Compute Kirchoff stress tensor

$$\boldsymbol{\tau}_{n+1} = J_{n+1}p_{n+1}\boldsymbol{I} + \boldsymbol{S}_{n+1}$$

6. Update

$$\bar{\varepsilon}_{n+1}^P = \bar{\varepsilon}_n^P + \Delta\gamma$$

$$\bar{\boldsymbol{B}}_{n+1}^e = \frac{\boldsymbol{S}_{n+1}}{G} + \frac{1}{3}tr\left(\bar{\boldsymbol{B}}_{n+1}^{e\,trial}\right)\boldsymbol{I}$$

$$\boldsymbol{C}_{n+1}^{P^{-1}} = \boldsymbol{F}_{n+1}^{-1}\boldsymbol{B}_{n+1}^{e}\boldsymbol{F}_{n+1}^{-T}$$

References

[1] L.B. Lucy, A numerical approach to the testing of the fission hypothesis, Astron. J. 82 (1977) 1013. https://doi.org/10.1086/112164.

[2] R.A. Gingold, J.J. Monaghan, Smoothed particle hydrodynamics: theory and application to non-spherical stars, Mon. Not. R. Astron. Soc. 181 (1977) 375–389. https://doi.org/10.1093/mnras/181.3.375.

[3] J.J. Monaghan, An introduction to SPH, Comput. Phys. Commun. 48 (1988) 89–96. https://doi.org/10.1016/0010-4655(88)90026-4.

[4] J.J. Monaghan, Smoothed Particle Hydrodynamics, Annu. Rev. Astron. Astrophys. 30 (1992) 543–574. https://doi.org/10.1146/annurev.aa.30.090192.002551.

[5] J.J. Monaghan, Smoothed Particle Hydrodynamics and Its Diverse Applications, Annu. Rev. Fluid

Mech. 44 (2012) 323–346. https://doi.org/10.1146/annurev-fluid-120710-101220.

[6] W.K. Liu, Y. Chen, S. Jun, J.S. Chen, T. Belytschko, C. Pan, R.A. Uras, C.T. Chang, Overview and applications of the reproducing Kernel Particle methods, Arch. Comput. Methods Eng. 3 (1996) 3–80. https://doi.org/10.1007/BF02736130.

[7] J.-S. Chen, S. Yoon, H.-P. Wang, W.K. Liu, An improved reproducing kernel particle method for nearly incompressible finite elasticity, Comput. Methods Appl. Mech. Eng. 181 (2000) 117–145. https://doi.org/10.1016/S0045-7825(99)00067-5.

[8] B. Nayroles, G. Touzot, P. Villon, Generalizing the finite element method: Diffuse approximation and diffuse elements, Comput. Mech. 10 (1992) 307–318. https://doi.org/10.1007/BF00364252.

[9] T. Belytschko, Y.Y. Lu, L. Gu, Element-free Galerkin methods, Int. J. Numer. Methods Eng. 37 (1994) 229–256. https://doi.org/10.1002/nme.1620370205.

[10] T. Belytschko, D. Organ, Y. Krongauz, A coupled finite element-element-free Galerkin method, Comput. Mech. 17 (1995) 186–195. https://doi.org/10.1007/BF00364080.

[11] T. Belytschko, Y. Krongauz, D. Organ, M. Fleming, P. Krysl, Meshless methods: An overview and recent developments, Comput. Methods Appl. Mech. Eng. 139 (1996) 3–47. https://doi.org/10.1016/S0045-7825(96)01078-X.

[12] T. Belytschko, M. Fleming, Smoothing, enrichment and contact in the element-free Galerkin method, Comput. Struct. 71 (1999) 173–195. https://doi.org/10.1016/S0045-7949(98)00205-3.

[13] J. Bonet, T.-S.L. Lok, Variational and momentum preservation aspects of Smooth Particle Hydrodynamic formulations, Comput. Methods Appl. Mech. Eng. 180 (1999) 97–115. https://doi.org/10.1016/S0045-7825(99)00051-1.

[14] T. Rabczuk, T. Belytschko, S.P. Xiao, Stable particle methods based on Lagrangian kernels, Comput. Methods Appl. Mech. Eng. 193 (2004) 1035–1063. https://doi.org/10.1016/j.cma.2003.12.005.

[15] I. Alfaro, J. Yvonnet, E. Cueto, F. Chinesta, M. Doblare, Meshless methods with application to metal forming, Comput. Methods Appl. Mech. Eng. 195 (2006) 6661–6675. https://doi.org/10.1016/j.cma.2004.10.017.

[16] S. Xiong, J.M.C. Rodrigues, P.A.F. Martins, On background Cells during the Analysis of Bulk Forming Processes by the Reproducing Kernel Particle Method, Comput. Mech. 40 (2007) 233–247. https://doi.org/10.1007/s00466-006-0088-z.

[17] S. Xiong, C.S. Li, J.M.C. Rodrigues, P.A.F. Martins, Steady and non-steady state analysis of bulk forming processes by the reproducing kernel particle method, Finite Elem. Anal. Des. 41 (2005) 599–614. https://doi.org/10.1016/j.finel.2004.10.003.

[18] E. Cueto, F. Chinesta, Meshless methods for the simulation of material forming, Int. J. Mater. Form. 8 (2015) 25–43. https://doi.org/10.1007/s12289-013-1142-y.

[19] R.O.S.S. Costa, J. Belinha, R.M. Natal Jorge, D.E.S. Rodrigues, Optimizing a meshless method for the simulation of the extrusion of non-Newtonian materials, Int. J. Mech. Sci. 208 (2021) 106688. https://doi.org/10.1016/j.ijmecsci.2021.106688.

[20] M.-H. Lee, W.-H. Chen, Y. Mao, A Layer-Arranged Meshless Method for the Simulation of Additive Manufacturing with Irregular Shapes, Micromachines 12 (2021) 674. https://doi.org/10.3390/mi12060674.

[21] Z.L. Zhang, M. Afrasiabi, M. Bambach, A meshless computational framework for studying cold spray additive manufacturing including large numbers of powder particles with diverse characteristics, Sci. Rep. 14 (2024) 11393. https://doi.org/10.1038/s41598-024-62091-2.

[22] A. Chhillar, R. Singh, P. Sharma, A.N.M. Asiri, S. Islam, A. Razak, Elastoplastic Analysis of Metallic Parts Employing a Meshless Method, ACS Omega 8 (2023) 33493–33513. https://doi.org/10.1021/acsomega.3c03295.

[23] Daniel Rodrigues, Jorge Belinha, Renato Natal Jorge, THE RADIAL POINT INTERPOLATION METHOD IN THE BENDING ANALYSIS OF SYMMETRIC LAMINATES USING HSDTS, (2021).

[24] C.H. Lee, A.J. Gil, A. Ghavamian, J. Bonet, A Total Lagrangian upwind Smooth Particle Hydrodynamics algorithm for large strain explicit solid dynamics, Comput. Methods Appl. Mech. Eng. 344 (2019) 209–250. https://doi.org/10.1016/j.cma.2018.09.033.

[25] C.H. Lee, A.J. Gil, G. Greto, S. Kulasegaram, J. Bonet, A new Jameson–Schmidt–Turkel Smooth Particle Hydrodynamics algorithm for large strain explicit fast dynamics, Comput. Methods Appl. Mech. Eng. 311 (2016) 71–111. https://doi.org/10.1016/j.cma.2016.07.033.

[26] C.H. Lee, A.J. Gil, O.I. Hassan, J. Bonet, S. Kulasegaram, A variationally consistent Streamline Upwind Petrov–Galerkin Smooth Particle Hydrodynamics algorithm for large strain solid dynamics, Comput. Methods Appl. Mech. Eng. 318

(2017) 514–536. https://doi.org/10.1016/j.cma.2017.02.002.

[27] J. Bonet, S. Kulasegaram, Correction and stabilization of smooth particle hydrodynamics methods with applications in metal forming simulations, Int. J. Numer. Methods Eng. 47 (2000) 1189–1214. https://doi.org/10.1002/(SICI)1097-0207(20000228)47:6<1189::AID-NME830>3.0.CO;2-I.

[28] J. Bonet, C.H. Lee, A.J. Gil, A. Ghavamian, A first order hyperbolic framework for large strain computational solid dynamics. Part III: Thermo-elasticity, Comput. Methods Appl. Mech. Eng. 373 (2021) 113505. https://doi.org/10.1016/j.cma.2020.113505.

[29] P.R.R. de Campos, A.J. Gil, C.H. Lee, M. Giacomini, J. Bonet, A New Updated Reference Lagrangian Smooth Particle Hydrodynamics algorithm for isothermal elasticity and elasto-plasticity, Comput. Methods Appl. Mech. Eng. 392 (2022) 114680. https://doi.org/10.1016/j.cma.2022.114680.

[30] J. Bonet, A.J. Gil, C.H. Lee, M. Aguirre, R. Ortigosa, A first order hyperbolic framework for large strain computational solid dynamics. Part I: Total Lagrangian isothermal elasticity, Comput. Methods Appl. Mech. Eng. 283 (2015) 689–732. https://doi.org/10.1016/j.cma.2014.09.024.

[31] A.J. Gil, C.H. Lee, J. Bonet, R. Ortigosa, A first order hyperbolic framework for large strain computational solid dynamics. Part II: Total Lagrangian compressible, nearly incompressible and truly incompressible elasticity, Comput. Methods Appl. Mech. Eng. 300 (2016) 146–181. https://doi.org/10.1016/j.cma.2015.11.010.

[32] J. Haider, C.H. Lee, A.J. Gil, J. Bonet, A first-order hyperbolic framework for large strain computational solid dynamics: An upwind cell centred Total Lagrangian scheme, Int. J. Numer. Methods Eng. 109 (2017) 407–456. https://doi.org/10.1002/nme.5293.

[33] C.H. Lee, P.R. Refachinho de Campos, A.J. Gil, M. Giacomini, J. Bonet, An entropy-stable updated reference Lagrangian smoothed particle hydrodynamics algorithm for thermo-elasticity and thermo-visco-plasticity, Comput. Part. Mech. 10 (2023) 1493–1531. https://doi.org/10.1007/s40571-023-00564-3.

[34] H. Badnava, C.H. Lee, S.H. Nourbakhsh, P.R. Refachinho de Campos, A stabilised Total Lagrangian Element-Free Galerkin method for transient nonlinear solid dynamics, Comput. Mech. (2024). https://doi.org/10.1007/s00466-024-02507-y.

[35] S. Kobayashi, S.-I. Oh, T. Altan, Metal Forming and the Finite-Element Method, Oxford University Press, 1989. https://doi.org/10.1093/oso/9780195044027.001.0001.

[36] Industrieverband Deutscher Schmieden, Simulation in the Forging Industry, Hagen, Germany, 2006.

[37] T.B.J. Di Giusto, C.H. Lee, A.J. Gil, J. Bonet, M. Giacomini, A first-order hyperbolic arbitrary Lagrangian Eulerian conservation formulation for non-linear solid dynamics, Int. J. Numer. Methods Eng. (2024). https://doi.org/10.1002/nme.7467.

[38] J. Bonet, A.J. Gil, R.D. Wood, Nonlinear Solid Mechanics for Finite Element Analysis: Dynamics, Cambridge University Press, 2021. https://doi.org/10.1017/9781316336083.

[39] E.A. de Souza Neto, D. Perić, D.R.J. Owen, Computational Methods for Plasticity, Wiley, 2008. https://doi.org/10.1002/9780470694626.

[40] N. Abboud, G. Scovazzi, Elastoplasticity with linear tetrahedral elements: A variational multiscale method, Int. J. Numer. Methods Eng. 115 (2018) 913–955. https://doi.org/10.1002/nme.5831.

[41] F. Armero, E. Love, An arbitrary Lagrangian–Eulerian finite element method for finite strain plasticity, Int. J. Numer. Methods Eng. 57 (2003) 471–508. https://doi.org/10.1002/nme.684.